molecules

MDPI

Article

Bayesian Optimization-Assisted Synthesis of High Quantum Yield Boron-Doped Carbon Quantum Dots for Glutathione Selective Determination via Potassium Dichromate-Mediated Fluorescence "Off–On" Switch and Cell Imaging

Jianhao Xin [1,*,†], Shuqing Jiang [1,†], Rong Liu [1,2], Jianli Wu [1,*], Liyan Li [1], Lina Fu [1], Jianhua Xing [3], Xin Lv [1] and Rong Pang [1]

[1] School of Medicine, Huanghe Science and Technology University, Zhengzhou 450063, China; hkdyxysxb@163.com (S.J.); 18234323605@139.com (R.L.); lly@hhstu.edu.cn (L.L.); nilk4@163.com (L.F.); m17518990282@163.com (X.L.); pangrong1987@163.com (R.P.)
[2] School of Life Sciences, Henan University, Kaifeng 475004, China
[3] Henan Xintai Pharmaceutical Co., Ltd., Zhumadian 463000, China; xingjianhua1968@163.com
* Correspondence: 200703029@hhstu.edu.cn (J.X.); wjl@hhstu.edu.cn (J.W.)
† These authors contributed equally to this work.

Abstract

Boron-doped carbon dots (B-CDs) with high quantum yield (QY) were rationally synthesized via a hydrothermal method assisted by Bayesian optimization with Gaussian process regression. Sobol sensitivity analysis quantitatively revealed the dominant precursor factors and their interactive effects on QY, providing mechanistic understanding of boron doping. Under the optimized precursor mass ratio, the as-prepared B-CDs achieved a QY of 51.84%. The material was characterized by UV–Vis spectroscopy, FTIR, XRD, XPS, TEM, Raman spectroscopy and Zeta potential. Investigation of the quenching process of CrO-B-CDs revealed that the quenching behavior is attributed to static quenching mainly induced by oxidation of surface hydroxyl groups, demonstrating that abundant surface hydroxyl groups are the key fluorescence source of B-CDs. Benefiting from this surface-quenching effect triggered by potassium dichromate, a CrO-B-CD "off–on" fluorescent nanoprobe was fabricated for glutathione detection. The sensor exhibited a linear detection range of 0–16.0 μM ($R^2 = 0.997$) and a limit of detection as low as 24.0 nM at pH 6.0 with a reaction time of 2 min. Satisfactory recoveries were obtained for GSH quantification in human serum samples. Moreover, B-CDs displayed favorable biocompatibility and excellent photostability, enabling effective fluorescence imaging in HeLa cells. This study offers a data-driven strategy for fabricating high-performance carbon dots and presents a promising nanosensor for biosensing and bioimaging.

Keywords: boron-doped CDs; Bayesian optimization; fluorescence turn-on probe; detection of glutathione; bioimaging

Check for updates

Academic Editor: Takuya Terai

Received: 19 October 2026
Revised: 9 November 2026
Accepted: 24 November 2026
Published: 26 November 2026

Copyright: © 2026 by the authors. Licensee MDPI, Basel, Switzerland. This article is an open access article distributed under the terms and conditions of the Creative Commons Attribution (CC BY) license.

1. Introduction

Glutathione (GSH), also termed γ-L-glutamyl-L-cysteinylglycine, is a well-known non-protein thiol antioxidant consisting of glutamate, cysteine and glycine residues [1]. GSH is closely associated with multiple major diseases such as diabetes, Alzheimer's disease and cancer [2]. A variety of analytical approaches have been established for the quantification of GSH, including electrochemistry [3,4], spectrophotometry [5], capillary electrophoresis [6], fluorescence spectroscopy [7], and high-performance liquid chromatography (HPLC) [8].

Among these methods, fluorescence detection stands out due to its simple operation, high sensitivity, low sample consumption, and convenient real-time signal readout, which renders it highly suitable for GSH sensing [9].

As a fluorescent nanoprobe, carbon dots (CDs) have been widely researched over the last several years owing to their superior optical characteristics, high photostability, low toxicity, and versatile surface functionalization capabilities [10,11]. Recently, CDs have shown strong potential in many areas, such as drug delivery, bioimaging, biosensing and optoelectronic devices [12–14]. However, carbon dots often have a relatively insufficient quantum yield (QY) and suboptimal surface activity; thus, they are not suitable for high-sensitivity detection and cellular imaging at present [15,16].

Therefore, to address the above problems, heteroatom doping has begun to be used to tune the electronic structure and surface chemistry of CDs and thus improve their photoluminescence (PL) performance [17,18]. Nitrogen and sulfur are among the above options. The size mismatch of sulfur is relatively large, and nitrogen has lone pairs that donate electron density; together, they open new radiative paths [19–21]. Boron doping also increases this. B-CDs generally have higher quantum yields than other CDs, and their emission can be tuned across the entire visible light spectrum; thus, they are suitable for sensing and live-cell imaging [22–31].

The aforementioned advantages are not the only reasons, and the traditional one-variable-at-a-time (OVAT) method for tuning synthesis parameters often fails to consider the interactions among different experimental variables, thereby limiting the performance of the material [25]. Synthesis of B-CDs is about navigating a high-dimensional space; precursors, temperature and reaction time are all non-linearly related to the final QY. Therefore, a more intelligent optimization strategy is required to search this space efficiently and find the optimal synthesis conditions [26–28].

Bayesian optimization has recently shown some promise in the discovery of new materials and the optimization of synthesis routes [32]. A Gaussian process (GP) regression is used as a substitute model for this. It can adjust the ratio of exploration to exploitation dynamically, thus reaching a near-optimal solution without needing to conduct a large number of experiments [33]. The two reasons for the data-driven approach are to find the most reasonable synthesis conditions and to identify which parameters are influenced by it and how these parameters are interconnected using Sobol analysis [34]. Based on the above thinking, carbon dot synthesis has moved from a trial-and-error approach to a more rational design-oriented strategy.

Herein, we rationally fabricate high-QY boron-doped carbon dots via a hydrothermal route guided by Bayesian optimization. After systematic structural and optical characterizations, a potassium dichromate mediated "off–on" fluorescent nanoprobe is constructed for sensitive GSH determination. The sensing performance is evaluated in human serum samples, and the favorable biocompatibility of B-CDs is further validated for HeLa cell fluorescence imaging. This work demonstrates a data-oriented paradigm for rational carbon dot design and provides a promising fluorescent nanoplatform for biosensing and bioimaging applications.

2. Results and Discussion

2.1. Bayesian Optimization of Carbon Quantum Dot Synthesis

Extensive preliminary experimental investigations identified 140 °C and 9 h as the optimal synthesis temperature and duration, respectively. In this work, Bayesian optimization (BO) with a Gaussian process (GP) surrogate model was employed to optimize the synthetic feedstocks of B-CDs for the maximization of QY. Citric acid (CA), borax and urea were selected as the three key precursors serving as input variables, with QY defined as the

objective function. To construct the initial dataset, a total of 77 experimental runs were carried out, covering a broad compositional range: CA (0.105–0.384 g), borax (0.038–0.361 g) and urea (0–0.380 g) (The experimental data of the quantum yield and the programming code for Bayesian optimization are provided in the Supplementary Materials).

A Matérn 3/2 kernel and white noise were selected for the GP model to account for experimental noise. The fit was very good: $R^2 = 0.9769$, and the root mean square error (RMSE) was 0.0116 (Figure 1g). Thus, it can be concluded that the surrogate model accurately represents the complex non-linear relationships among synthesis parameters and QY. Figure 1h is the residual analysis. The residuals are randomly distributed around zero within a ±5% error band, and there is no systematic bias. Therefore, it can be used reliably.

Next, Bayesian optimization was employed to find the global optimum of the parameter space. The Expected Improvement (EI) acquisition function was selected to balance exploration and exploitation by considering both a high predicted QY and a large prediction uncertainty. The optimization converged to a composition of citric acid (0.210 g), borax (0.120 g), and urea (0.190 g), and a predicted QY of 51.6% was achieved (Figure 1a–c,e). This predicted optimum was close to our best experimental result (QY = 51.9%). In other words, our experimental design has covered the high-performance region reasonably well. The highest reported QY for boron-doped carbon quantum dots in the literature is 9.7% lower than this value [30]. The QYs, precursor systems, and spectral and sensing properties of previously reported B-doped CDs are systematically compared in Table S1 (QY range: 10.4–46.8%). To the best of our knowledge, the value achieved here is among the highest reported for hydrothermally derived B-doped CDs used in sensing applications.

As shown in the response surface plots (Figure 1a–c), the precursors have different interaction characteristics. As shown in Figure 1b, the optimum ridge of the CA–urea interaction is visible. Therefore, urea-doping has improved the QY of B-CDs; however, an optimal amount of a carbon source is still needed. On the other hand, too much borax (>0.20 g) reduces QY (Figure 1c), probably because it causes excessive cross-linking or over-passivation of the surface. Sensitivity analysis (Figure 1f) shows that close to the optimum, urea concentration and citric acid have relatively high impacts. Borax is relatively forgiving and performs well in the range of 0.10–0.15 g.

The uncertainty of the GP prediction at the optimal point was determined to be ±0.04 (2σ), as shown in Figure 1d. Therefore, we have a confidence bound to verify through experiments. As shown in the Expected Improvement plot (Figure 1e), the optimum we have found is indeed a global maximum in the region we have explored. This is evidenced by the EI values approaching zero, indicating that the optimization algorithm has converged.

Thus, Bayesian optimization has helped us explore a high-dimensional parameter space with only a few trials, thereby reducing the amount of labor input in a typical trial-and-error method. Accordingly, the composition determined in the optimization, namely citric acid (0.210 g), borax (0.120 g) and urea (0.190 g), was chosen for the following experiments. To further verify the reproducibility of this optimized synthetic protocol, five independent replicate syntheses were carried out with this formulation, and the mean quantum yield obtained was 51.84%; thus, it was selected as the optimal preparation condition for the rest of this study.

2.2. Characterization of the Morphology and Structure of B-CDs

TEM measurements were carried out to analyze the particle morphology and interior structure of the as-prepared material. It exhibited that B-CDs are spherical particles with good monodispersity (Figure 2a). The HRTEM image (Figure 2b) revealed an average observable interplanar spacing of 0.22 nm, matching the (002) facet of graphitic carbon. Figure 2c gives the size distribution histogram. Most particles fall between 1.0 and 4.0 nm, with a mean diameter of 2.28 nm.

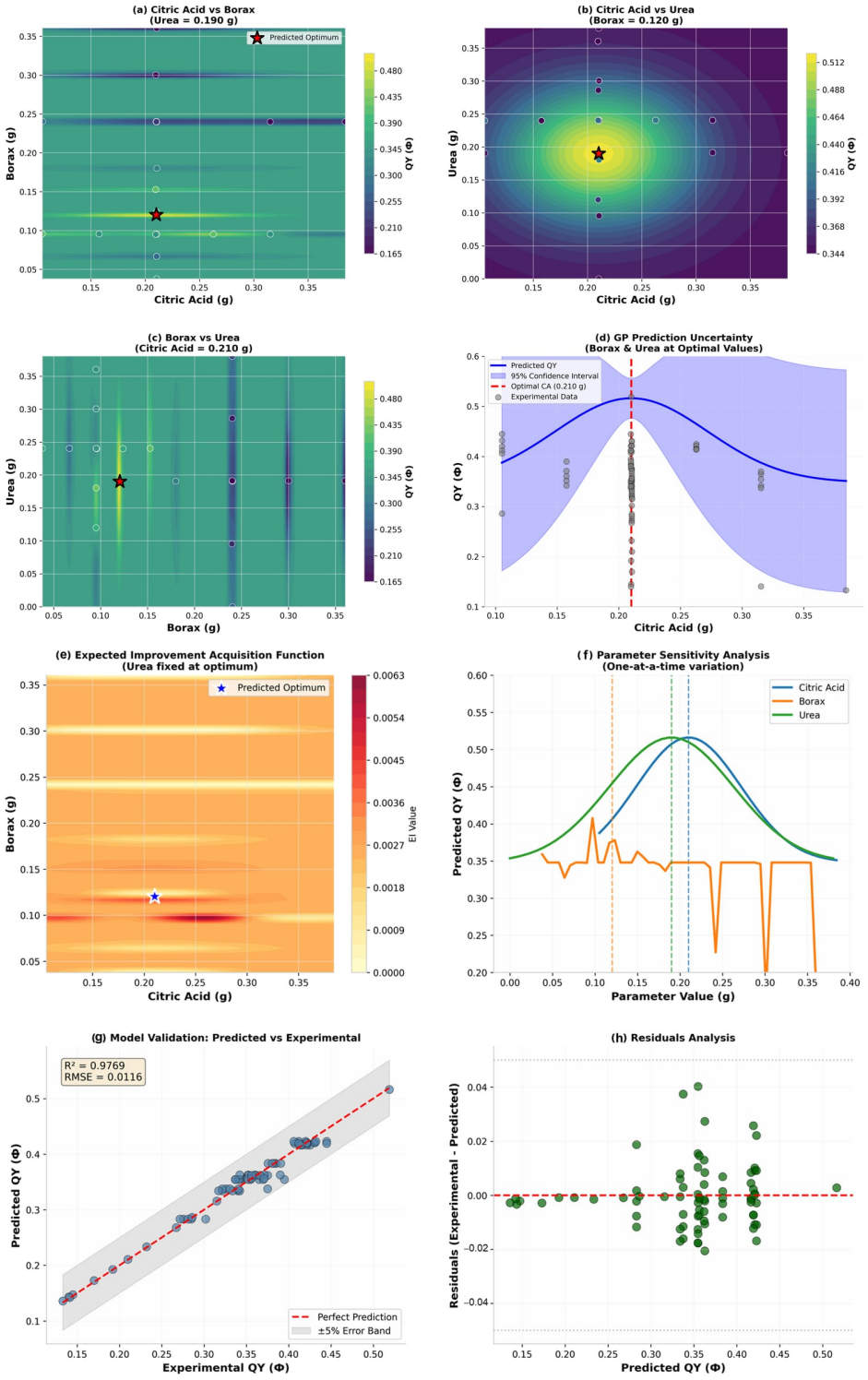

Figure 1. Bayesian optimization results for B-CD synthesis: response surfaces from the GP model. In each panel, two precursors are fixed at their optimal values while the third varies: (**a**) citric acid vs. borax (urea = 0.190 g); (**b**) citric acid vs. urea (borax = 0.120 g); (**c**) borax vs. urea (citric acid = 0.210 g; (**d**) GP prediction uncertainty vs. citric acid (other parameters at their optima). Red stars mark the predicted optimal composition. (**e**) Expected improvement landscape. Urea = 0.190 g (optimal). Star: predicted optimum; (**f**) sensitivity: one precursor changed at a time; others fixed at optimal; the vertical dotted line indicates the optimal dosage. (**g**) model validation: predicted vs. experimental QY. R^2 = 0.9769, RMSE = 0.0116; blue dots represent experimental data points. (**h**) residuals: green dots are residual values, and the red horizontal dotted line marks the zero residual baseline; residuals are randomly distributed without systematic bias.

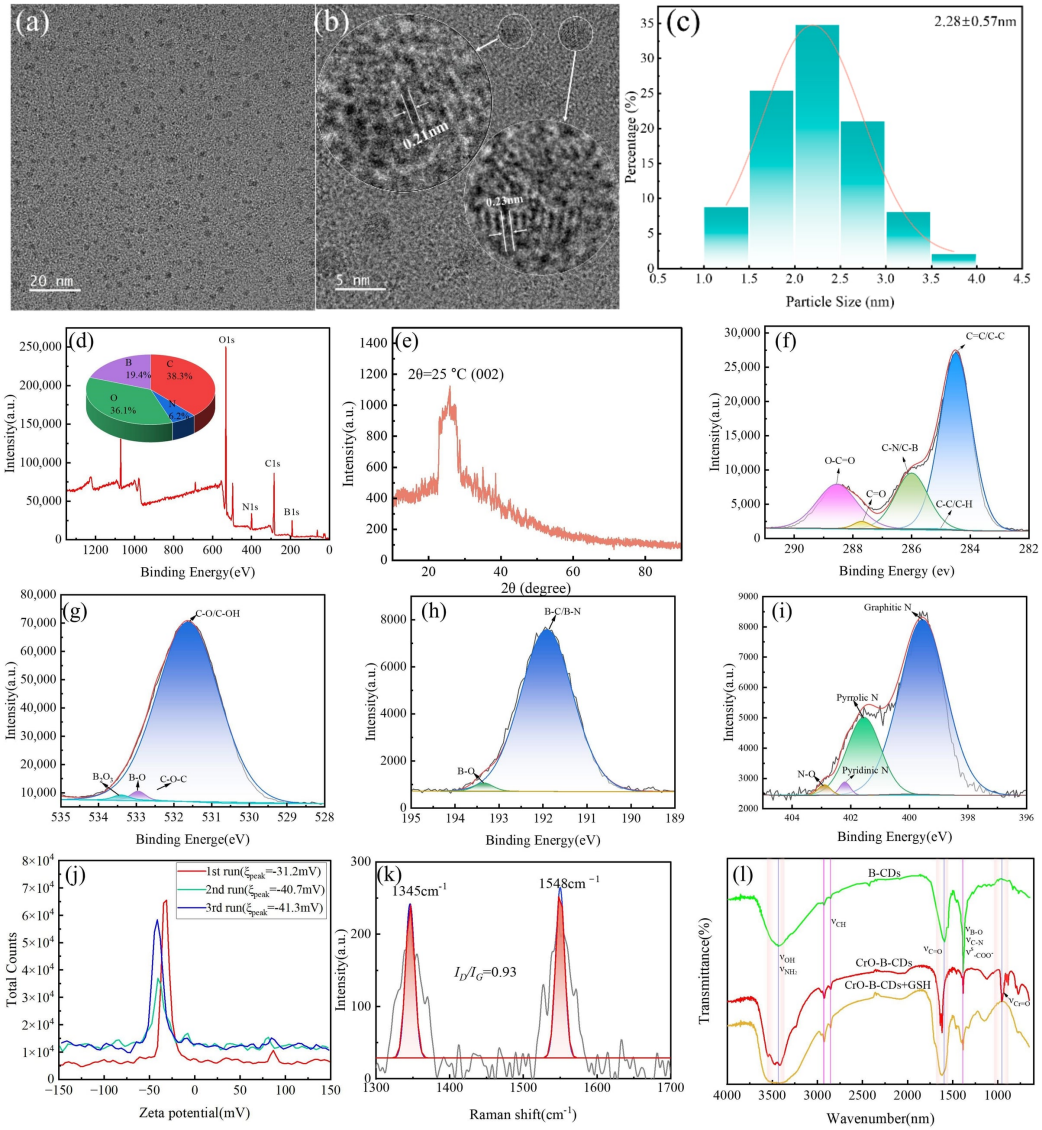

Figure 2. (**a**) TEM of B-CDs; scale bar: 20 nm. (**b**) HRTEM image showing lattice fringes; scale bar: 5 nm. (**c**) Particle diameter distribution histogram of B-CDs.The orange curve represents the Gaussian fitting. (**d**) Survey spectrum (inset: elemental mapping images). (**e**) XRD spectrum of B-CDs and XPS spectrum of B-CDs. (**f**) C 1s spectrum. (**g**) B 1s spectrum. (**h**) N 1s spectrum. (**i**) O 1s spectrum. (**j**) Zeta potential. (**k**) Raman spectrum. (**l**) FTIR spectrum.

Energy-dispersive X-ray spectroscopy analysis shows that the product contains B, N, C, and O. Figure 2d reveals the elemental mapping images. It is evident that the elements B, N, C, and O were uniformly spread throughout B-CDs. B, N, and C were constituent elements of B-CDs, while O likely derived from the chemical groups present on the surface of B-CDs. To identify the chemical groups on the surface of B-CDs, Figure 2l displays the FTIR results. The spectra verify that CDs are successfully doped with boron. The doping introduces numerous chemical groups on the surface of B-CDs, thereby enhancing QY. The XRD pattern of the B-CDs (Figure 2e) shows a wide and scattered diffraction peak in the 2θ range of 25°, indexed to the (002) plane of graphitic carbon. Notably, no diffraction features associated with crystalline boron phases are detected, indicating that the boron is atomically dispersed within the carbon lattice rather than forming separate phases. To additionally clarify the elemental composition of the acquired sample, analysis was conducted via XPS. The survey XPS spectrum of B-CDs (Figure 2d) showed the peaks at 284.4, 399.55, 191.95

and 531.6 eV. They are assigned to C 1s, N 1s, B 1s and O 1s in sequence. The atomic contents were about 38.27% (C), 6.25% (N), 19.42% (B), and 36.07% (O), respectively.

The high-resolution C 1s spectrum was deconvoluted into five characteristic peaks. The dominant one, located at 284.6 eV, was assigned to C=C/C–C bonds originating from the graphitic carbon framework, while a component at 285.0 eV corresponded to aliphatic C–C/C–H species. At 286.0 eV, the peak was attributed to C–N/C–B bonds, confirming that nitrogen and boron had been covalently incorporated into the carbon matrix. Further peaks appeared at 287.2 eV and 288.6 eV, which were ascribed to carbonyl (C=O) and carboxyl (O–C=O) groups, respectively. These assignments point to a considerable number of oxygen-containing functional groups on the surface of the B-CDs (Figure 2f). The O 1s spectrum was fitted into four peaks. A major contribution at 531.4 eV came from C–O/C–OH moieties, suggesting abundant hydroxyl sites. A C–O–C ether signal was observed at 532.3 eV. Crucially, the component at 532.9 eV, assigned to B–O–C, provided direct evidence for boron doping. A weak peak at 533.9 eV was attributed to B–O–B species, likely from B_2O (Figure 2g). In the B 1s spectrum (Figure 2h), two components could be resolved. The main peak, centered at 192.0 eV, was assigned to B–C/B–N bonds, reinforcing the picture of covalent boron incorporation. The signal at 193.4 eV, associated with B–O environments, matched well with the boron-oxide-related features already seen in the O 1s spectrum. Deconvolution of the N 1s spectrum gave four nitrogen configurations: graphitic N at approximately 400.5 eV, pyrrolic N at 401.8 eV, pyridinic N at 402.8 eV, and N–O at 403.8 eV. Graphitic N dominated the spectrum, reflecting efficient nitrogen doping through urea pyrolysis (Figure 2i).

Zeta-potential measurements further corroborate the surface chemistry. B-CDs exhibit negative Zeta-potential values in the range of −31.2 to −41.3 mV (Figure 2j), a charge that originates from surface carboxyl and hydroxyl groups. This substantial negative potential endows the carbon dots with favorable colloidal stability in water. The Raman spectrum of the B-CDs (Figure 2k) was deconvoluted into two characteristic bands located at 1345 and 1548 cm^{-1}, corresponding to the D band (disorder-induced vibrations of sp^3-type defects) and the G band (in-plane stretching of sp^2-hybridized carbon), respectively. The integrated intensity ratio, $I_D/I_G = 0.93$, points to a carbon framework that is well graphitized yet rich in structural imperfections introduced by heteroatom doping. It is precisely these defect sites that are expected to serve as fluorescent emissive centers, thereby accounting for the pronounced photoluminescence of the B-CDs.

Overall, the XPS analysis, together with the zeta-potential and Raman results, demonstrates that both boron and nitrogen are covalently doped into the carbon dot skeleton. The abundant polar oxygen-containing groups not only confer good aqueous dispersibility and colloidal stability but also contribute to the favorable fluorescence properties of the B-CDs.

2.3. Spectroscopic Properties of B-CDs and Mechanism

UV–Vis absorption imagery was employed to investigate the optical properties of B-CDs, as shown in Figure 3a. Under irradiation at 364 nm, the B-CDs dispersion (green) emitted bright turquoise fluorescence.

As shown in the fluorescence results in Figure 3b, B-CDs exhibit stronger fluorescence intensity. Obvious fluorescence quenching occurs upon the addition of potassium dichromate into the B-CDs dispersion. Subsequent addition of GSH leads to the recovery of fluorescence. According to the FTIR spectra in Figure 2l, the boron-doped B-CDs show a characteristic IR band at 1620 cm^{-1}. After introducing potassium dichromate, a new Cr=O related band appears at 950 cm^{-1}, revealing that potassium dichromate is reduced by B-CDs, and the Cr=O containing species are anchored on the material surface. The resulting product is therefore denoted as CrO-B-CDs. Comparing the FTIR spectra of B-CDs and

CrO-B-CDs, the original single band at 3460 cm^{-1} splits into two peaks assigned to primary amine groups. It is presumed that the oxidation or coordination of hydroxyl groups weakens the hydroxyl-related signal and makes the primary-amine peaks observable. Meanwhile, the C=O band at 1610 cm^{-1} also splits into doublets, which may originate from vibrational coupling between adjacent carbonyl groups caused by hydroxyl oxidation.

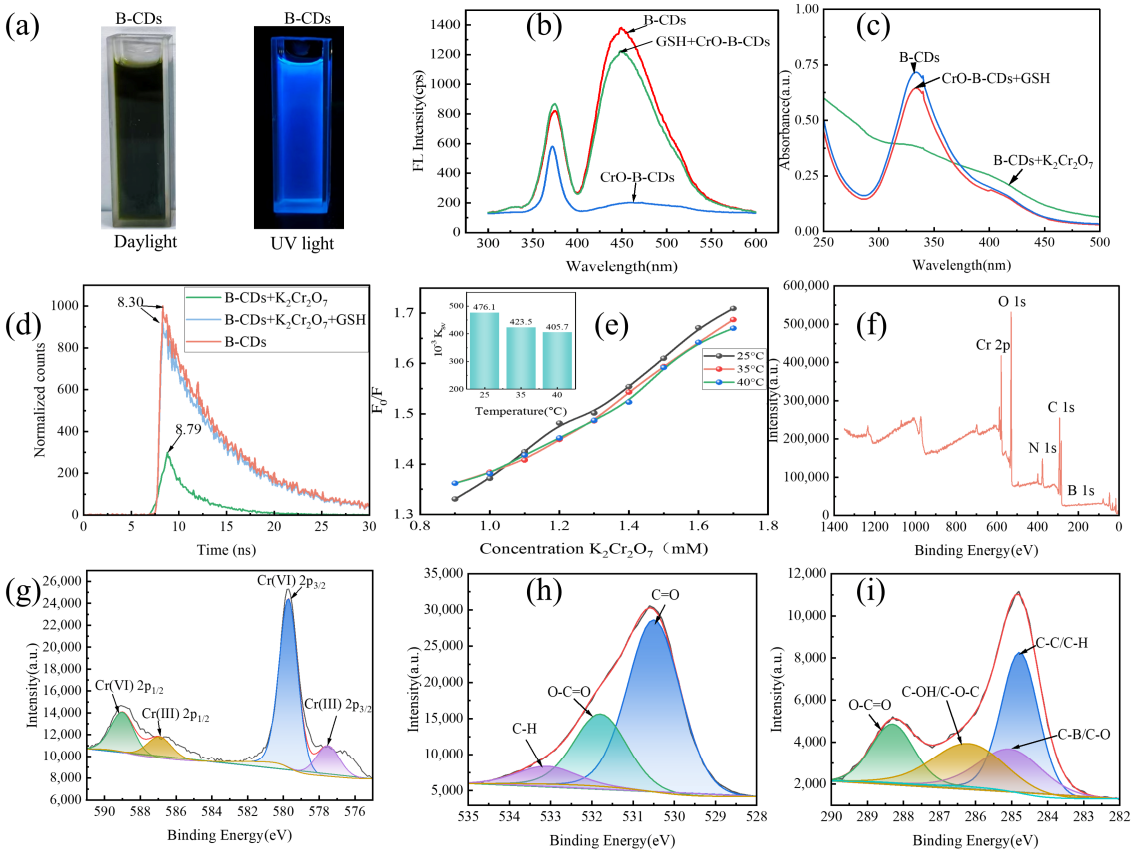

Figure 3. (**a**) Optical images in daylight and UV light. (**b**) Emission spectra of B-CDs, CrO-B-CDs and CrO-B-CDs + GSH. (**c**) UV absorption spectrum. (**d**) Fluorescence lifetimes of B-CDs and B-CDs + $K_2Cr_2O_7$. (**e**) Stern–Volmer plots of F_0/F versus $K_2Cr_2O_7$ concentration at 25 °C, 35 °C and 40 °C (inset: bar chart showing the corresponding Ksv values under different temperatures). XPS spectra of CrO-B-CDs: (**f**) Survey spectrum. (**g**) Cr 2p spectrum. (**h**) O 1s spectrum. (**i**) C 1s spectrum.

As illustrated in the UV–Vis absorption spectra (Figure 3c), the addition of $K_2Cr_2O_7$ induced an obvious alteration in the absorption profile of B-CDs, strongly implying the formation of a non-fluorescent ground-state complex between B-CDs and $K_2Cr_2O_7$. Time-resolved fluorescence decay spectra show that the fluorescence lifetime of B-CDs increased only slightly after introducing $K_2Cr_2O_7$ from 8.30 ns to 8.79 ns (Figure 3d). The slight increase in the average lifetime likely reflects the selective consumption of the more quenchable surface emissive sites, leaving a residual population with slightly reduced non-radiative decay rates. Combined with the Stern–Volmer analysis in Figure 3e, the quenching constant (Ksv) decreased with rising temperature. The above results indicate that the quenching behavior is mainly attributed to static quenching, which is mainly induced by the oxidation of surface hydroxyl groups on the B-CDs surface; minor contributions from inner-filter effects or photoinduced electron transfer cannot be strictly excluded but are not claimed here, as the combined absorption, lifetime, and surface-chemistry evidence supports static quenching as the dominant pathway. This implies that abundant surface hydroxyl groups

constitute a key source of fluorescence for B-CDs. Furthermore, fluorescence is recovered after adding GSH.

XPS measurements were performed to reveal the interaction between B-CDs and $K_2Cr_2O_7$. The full survey spectrum clearly identifies the characteristic peaks of B, C, N, O and Cr (Figure 3f), confirming the successful binding of chromium species onto the B-CDs surface after incubation with $K_2Cr_2O_7$. In the Cr 2p spectrum recorded after contact with $K_2Cr_2O_7$ (Figure 3g), the Cr $2p_{3/2}$ envelope is deconvoluted into two components at 577.3 and 579.1 eV, assigned to Cr (III) and Cr (VI), respectively, with a concomitant Cr $2p_{1/2}$ doublet at higher binding energy. Figure 3h,i display obvious binding energy shifts and an increased proportion of oxygen species, indicating the oxidation of surface hydroxyl groups. Combined with the FTIR spectra (Figure 2l), these results reveal that potassium dichromate preferentially oxidizes the surface hydroxyl groups of B-CDs and is concomitantly reduced to Cr (III). Cr (VI) species are anchored on the surface of carbon dots via Cr = O bonds, whereas the generated Cr (III) is adsorbed onto the carbon dot surface. Upon the addition of GSH, the surface-bound Cr (VI) is reduced, and B-CDs are released. The recovered B-CDs exhibit an FTIR profile identical to that of pristine B-CDs (Figure 2l), accompanied by fluorescence restoration (Figure 3d).

2.4. Optimization of Analytical Conditions

Figure 4a shows the excitation spectrum (recorded with the emission monitored at 450 nm) and the emission spectrum (recorded under 364 nm excitation), together with the emission spectra recorded at excitation wavelengths from 250 to 500 nm. The emission maximum remains at 450 nm throughout the 250–400 nm excitation range, while the intensity reaches a maximum at 364 nm excitation, confirming 364/450 nm as the optimal wavelength pair. All subsequent fluorescence measurements were performed at this pair. To engineer a high-performance fluorescence nanoprobe, we systematically investigated the influence of the $K_2Cr_2O_7$ concentration on the preparation of CrO-B-CDs nanocomposites at ambient temperature. As depicted in Figure 4b, the fluorescence spectra of the nanocomposites exhibit a distinct concentration-dependent quenching behavior upon incremental addition of $K_2Cr_2O_7$. The emission intensity of the B-CDs decreases progressively with rising $K_2Cr_2O_7$ levels and reaches a minimum at 3.16 μM, beyond which nearly no further quenching is observed—where the quenchable surface sites are essentially fully complexed (saturation of the fluorescence modulation), and no extra intensity decrease is observed.

Under the optimized concentration of $K_2Cr_2O_7$, the fluorescence intensities of both carbon dots and the CrO-B-CDs composite were measured across a pH range of 3 to 10. As displayed in Figure 4c, the difference in fluorescence intensity between the CrO-B-CDs composite and the reaction of GSH with CrO-B-CDs was most pronounced at pH 6.0, where the quenching efficiency reached its maximum. Moreover, the fluorescence intensity maintained good stability upon the B-CDs. Consequently, although the intrinsic fluorescence of B-CDs is stable over pH 4–8, the difference between the quenched and GSH-recovered signals—the analytical response window—is maximal at pH 6.0, which was therefore selected as the working pH.

After adding 10 μM of GSH for 2 min, the PL of the CrO-B-CDs increased to its maximum value, because the redox reaction was completed. So, 2 min is the optimal interaction time (Figure 4d).

2.5. Analytical Performance of CrO-B-CDs Fluorescence Probe for GSH

Therefore, based on the CrO-B-CDs fluorescence probe, we constructed a simple and sensitive "off–on" fluorescent sensor to detect GSH. Within the linear range, the fluorescence intensity corresponding to different GSH concentrations can be seen in Figure 4e.

The corresponding linear equation for GSH detection was F = 141.8 C_{GSH} + 117.3 (μM, R^2 = 0.997), and the limit of detection (LOD) was 24.0 nM (S/N = 3). Beyond this range the response plateaus, because the finite amount of surface-bound Cr (VI) (fixed by the 3.16 μM $K_2Cr_2O_7$ used to prepare the probe) is fully reduced; the linear range is thus bounded by the quenching-agent loading, which in principle could be tuned to extend the range. Table 1 summarizes the comparison with current carbon dot-based methods for the determination of GSH in blood reported in previous studies [35–40]; the analytical performance of this work for GSH has better sensitivity and a relatively lower detection limit, which originates from the high fluorescence quantum yield of B-CDs obtained after Bayesian optimization.

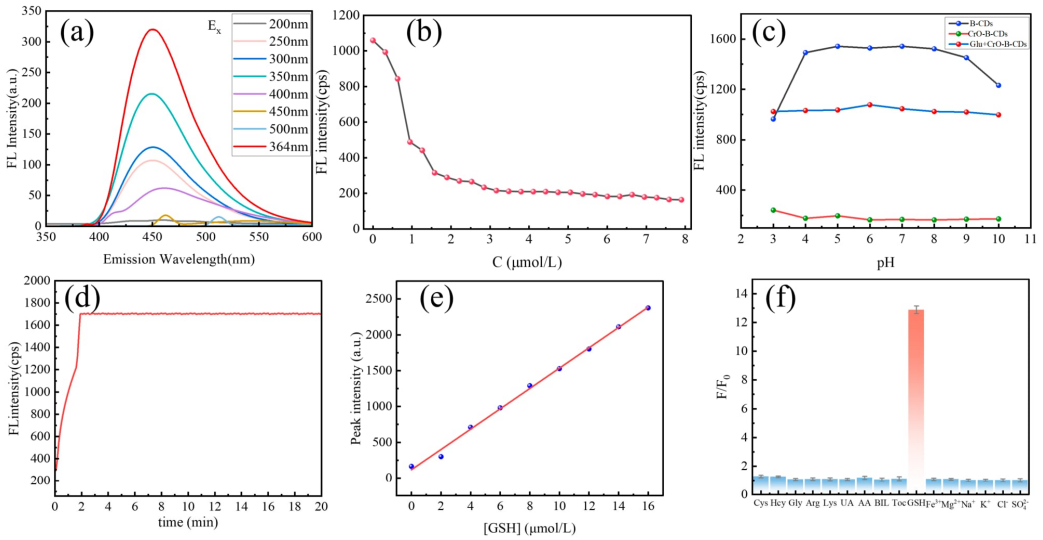

Figure 4. (**a**) Excitation and emission spectra. (**b**) Fluorescence intensity variation of B-CDs with increasing $K_2Cr_2O_7$ concentration. (**c**) pH-dependent fluorescence responses of B-CDs, CrO-B-CDs, and CrO-B-CDs after reaction with GSH in the pH range of 3–10. (**d**) Time-resolved fluorescence recovery behavior of CrO-B-CDs upon addition of GSH. (**e**) Linear calibration plot of fluorescence peak intensity versus GSH concentration. (**f**) Selectivity of the CrO-B-CDs probe for GSH against other potential interferents (Cys, Hcy, Gly, Arg, Lys, UA, AA, BIL, Tocs, Fe^{3+}, Mg^{2+}, Na^+, K^+, Cl^-, SO_4^{2-}).

Table 1. Comparisons of the analytical performance of the proposed B-CDs-based method with previously reported CDs-based methods for GSH detection in blood.

Precursors	QY	Methods	Linear Range	LOD	Reference
Citric acid (CA) + L-lysine	26.51%	Hg^{2+} off–GSH on	0–30 μM	0.104 μM	[35]
Anhydrous citric acid + 2-aminobenzimidazole	11.17%	Hg^{2+} off–GSH on	40–120 μM	3.43 μM	[36]
Soluble starch + citric acid		Peroxidase-mimic colorimetric detection	0.1–50 μM	0.05 μM	[37]
EDA + H_3PO_4	3.26%	Dual-mode: colorimetric and room-temperature phosphorescence (RTP) sensing	0.5–100 μM	0.14 μM	[38]
Wheatgrass juice + choline chloride–urea	36%	Hg^{2+} off–GSH on	0–5.5 μmol/L	43 nM	[39]
Grass carp fish scales	23.8%	Ag^+ off–GSH on	1.6–36 μg mL^{-1}	0.77 μg·mL^{-1}	[40]
Citric acid, borax, urea	51.84%	$K_2Cr_2O_7$ off–GSH on	0–16.0 μM	24.0 nM	This work

The interference from six essential amino acids, endogenous blood reducing agents (uric acid (UA), ascorbic acid (AA), bilirubin (BIL) and α-tocopherol (α-Toc)), and various metal ions (all concentrations were 14 μM) on the fluorescence signal of CrO-B-CDs system were investigated. As shown in Figure 4f, most of the tested substances caused negligible fluorescence recovery. In particular, cysteine and homocysteine, both of which contain sulfhydryl groups, also produced only weak fluorescence recovery. Nevertheless, as is known in biological systems, the physiological concentrations of cysteine and homocysteine are far lower than that of GSH; hence, the interference originating from cysteine and homocysteine is expected to exert a negligible effect on GSH detection during real sample analysis [41].

2.6. Applications

2.6.1. Detection of GSH in Actual Sample and Recovery

We investigated the practical application of the CrO-B-CDs probe for determining GSH levels by performing spike-and-recovery analyses in three human serum samples. The results showed recovery rates ranging from 93.23% to 106.4%, with relative standard deviations below 5.2%. These findings indicated the potential of the proposed method for GSH screening in real samples (Table 2).

Table 2. Recovery of GSH in samples.

Samples	Detected (mg/100 g)	Recovery (mg/100 g) ± RSD (%)		
		Added 15.00 mg/100 g	Added 30.00 mg/100 g	Added 45.00 mg/100 g
1	28.42 ± 0.16	35.82 ± 2.3	58.20 ± 3.4	75.11 ± 4.6
2	30.64 ± 0.21	43.54 ± 3.1	61.42 ± 2.8	78.82 ± 4.1
3	32.28 ± 0.24	46.41 ± 2.9	61.46 ± 4.3	82.18 ± 5.2

2.6.2. Cytotoxicity Measure and Cell Imaging of B-CDs

Given the potential of B-CDs as fluorescent probes for cell imaging, their biocompatibility and cytotoxicity were systematically evaluated using HeLa cells via the CCK-8 assay, which reflects cellular dehydrogenase-mediated metabolic activity and serves as a widely used indirect indicator of cell viability. The optical density (OD) was recorded at 450 nm, and the cell viability was calculated based on Equation (2). As presented in Figure 5a, the cell viability remained 91.02% at 125 μg mL^{-1} after 24 h incubation with B-CDs. These results indicate that B-CDs possess good biocompatibility and low cytotoxicity toward HeLa cells under the tested conditions, demonstrating their significant potential for biological applications.

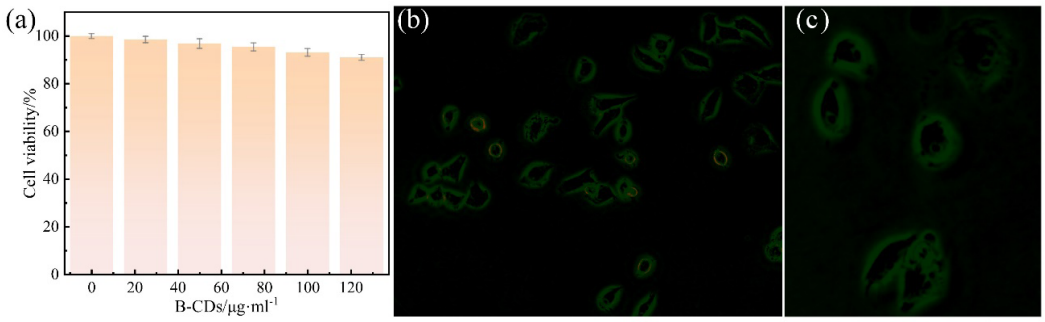

Figure 5. (**a**) Cytotoxicity studies of the B-CDs (24 h posttreatment) by the CCK-8 assay for HeLa cells; (**b**) the image acquired under dark field mode; (**c**) the magnified image.

Owing to their favorable low cytotoxicity and good biocompatibility, the cell imaging tests were carried out to additionally verify their potential for biological applications. The corresponding dark-field image (Figure 5b) displays strong blue and green fluorescence under excitation at 364 nm, which suggests that HeLa cells, as a tumor cell line, exhibit an irregular, elongated or spindle-shaped morphology with aberrant nuclear features—including nuclear enlargement, polymorphism, and notably prominent nucleoli (the magnified view is shown in Figure 5c). Benefiting from the high quantum yield achieved via Bayesian optimization, B-CDs exhibit enhanced brightness and yield sharper imaging performance compared with previously reported strategies [24–27]. In addition, the bright intracellular fluorescence indicates that B-CDs are readily internalized by HeLa cells. Considering their ultrasmall diameter (≈2.28 nm) and the precedent of similarly sized carbon dots, the internalization is likely associated with endocytosis; however, since the present evidence is based on fluorescence imaging, the precise uptake pathway warrants dedicated investigation and is not claimed here as an established fact. Since the cell morphology did not undergo remarkable alterations, the low cytotoxicity of B-CDs was further validated. Meanwhile, the fluorescence of labeled HeLa cells maintained stable intensity after one hour of sustained excitation, reflecting that B-CDs have superior photostability and are less prone to photobleaching. In consideration of this, the foregoing results demonstrate that B-CDs possess promising prospects for biological applications.

3. Materials and Methods

3.1. Materials

Analytical-grade chemicals were commercially obtained and employed without additional purification. Borax (sodium tetraborate decahydrate), citric acid, urea, 2-(2-methoxy-4-nitrophenyl)-3-(4-nitrophenyl)-5-(2,4-disulfophenyl)-2h-tetrazolium sodium salt (CCK-8), potassium dichromate ($K_2Cr_2O_7$), and quinine sulfate were obtained from Aladdin. (Shanghai, China). Sulfuric acid (H_2SO_4), N,N-Dimethylformamide (DMF), and MES buffer were purchased from Macklin (Shanghai, China). Dialysis bags (500 Da molecular weight cutoff) and 0.22 μm microporous membranes were supplied by Solarbio Science & Technology Co., Ltd. (Beijing, China). HeLa cells were acquired from Servicebio Technology Co., Ltd. (Wuhan, China). Aqueous solutions were prepared exclusively with Milli-Q ultra-pure water (resistivity of 18.2 MΩ·cm).

3.2. Preparation of B-CDs

B-CDs were generated through a hydrothermal process. In a typical procedure, 0.120 g of borax, 0.210 g of citric acid and 0.190 g of urea were mixed in 10 mL DMF under magnetic stirring for 10 min. Afterwards, the resulting dispersion was then placed into a Teflon-lined autoclave with a volume of 50 mL and maintained at 140 °C for 9 h in a constant-temperature oven. When the reaction was finished, the obtained dispersion was permitted to cool to ambient temperature on its own, and the larger particles were pelleted by centrifugation at 10,000 rpm for 15 min. The supernatant was passed through a 0.22 μm syringe filter and then loaded into a dialysis bag (500 Da) to get rid of the unreacted small molecules. Then, the purified B-CDs were ultimately obtained as a dry powder via freeze-drying and were kept at 4 °C until required.

3.3. QY Determination of B-CDs

Fluorescence spectra of individual samples were obtained by means of a Hitachi F-7100 fluorescence spectrophotometer (Tokyo, Japan) upon excitation at 364 nm. Furthermore, excitation and emission slit widths were both fixed at 5 nm. Quinine sulfate (QS) has a

quantum yield of approximately 54% in H_2SO_4 (0.1 M) at 364 nm and acted as the reference standard. The QY (Φ) of B-CDs was determined based on the subsequent formula.

$$\Phi_{CDs} = \Phi_R(I_{CDs}/I_R)(A_R/A_{CDs})(\eta_{CDs}/\eta_R)^2 \quad (1)$$

where 'Φ' denotes the QY, 'I' is the FL intensity, 'A' refers to the absorbance, and 'η' represents the solvent refractive index. The subscripts 'CDs' and 'R' correspond to B-CDs and the reference fluorophore with known QY, respectively.

3.4. Specificity of B-CDs

3.4.1. Preparation of CrO-B-CDs

First, 1.00 mL B-CDs dispersion (3 μg/mL) was transferred into a centrifuge tube filled with 1.5 mL of pH 6.0 MES buffer (0.10 mM). Subsequently, 1.0 mL of $K_2Cr_2O_7$ (3.16 μM) was introduced, and the mixture was made up to 5.0 mL with ultra-pure water. Then, the resulting mixture was subsequently ultrasonicated for 30 min, yielding a brownish-black colloidal suspension. The clarified CrO-B-CDs nanocomposite was obtained by centrifugation at 10,000 rpm for 15 min, washed with ultra-pure water for several cycles, and vacuum freeze-dried.

3.4.2. Fluorescence Sensing of GSH

First, 100 μL of GSH solution was mixed with 100 μL of CrO-B-CDs dispersion (100 μg/mL) in 200 μL of MES buffer (0.10 mM), yielding a total volume of 3.0 mL by ultra-pure water. The resulting mixture solution was then left to stand for 2 min at ambient temperature. Subsequently, fluorescence intensity was detected, and the selectivity was evaluated using potential substances including amino acids and some ions.

3.4.3. Actual Samples Analysis

Human serum samples were collected in accordance with the ethical principles of the Declaration of Helsinki (2013 revision), and the protocol was approved by the Biomedical Research Ethics Committee of Huanghe science and technology college (No. 2025–058).

Human serum samples and acetonitrile were mixed with a volume ratio of 1:1. After 3 min, the samples were centrifuged in a 10,000 rpm for 10 min to collect the supernatant, which was diluted 200 times with ultra-pure water. The resulting solutions were subjected to the GSH fluorescence-sensing assay in place of standard GSH samples.

3.5. Cytotoxicity Assay and Cellular Fluorescence Imaging of B-CDs

The CCK-8 assay was adopted to assess the cytotoxicity of B-CDs. HeLa cells were plated into 96-well plates at a seeding density of 5×10^3 cells per well. The cells were treated with B-CDs dispersions at contents of 0, 12.5, 25, 50, 100, and 125 μg/mL, with six replicate wells per concentration, after 24 h of incubation. Following another 24 h of culturing, 10 μL of 10% CCK-8 reagent was loaded to each well, and the plates were kept at 37 °C in the dark for 2 h. Subsequently, the absorbance at 450 nm (OD value) was recorded using a microplate reader. The cell viability was calculated according to the following formula:

$$\text{cellviability (\%)} = \left(\frac{OD_{treated}}{OD_{control}}\right) \times 100\% \quad (2)$$

Following the incubation of HeLa cells alone at 37 °C for 24 h, 125 μg/mL B-CDs were then introduced to the HeLa cells, and incubation continued for another 24 h. The cells were flushed with pH7.4 phosphate buffer solution to wash away unbound B-CDs and then fixed onto microscope slides using glycerol. Fluorescence images were acquired with a Nikon Ts2FL inverted fluorescence microscope (Nikon Corporation, Tokyo, Japan), with excitation at 364 nm.

4. Conclusions

In summary, we developed a fluorescent sensing method for the sensitivity detection of GSH in human serum samples and cell imaging, employing high QY B-CDs synthesized hydrothermally and optimized by Bayesian optimization combined with Gaussian process regression. Under optimized precursor proportions, the as-synthesized B-CDs achieved a remarkable quantum yield of 51.84%. Benefiting from the surface-quenching effect induced by potassium dichromate, a CrO-B-CDs "off–on" fluorescent nanoprobe was constructed for GSH detection. The method achieved an LOD of 24.0 nM, demonstrating suitable analytical sensitivity for clinical detection, with recovery values ranging from 93.23% to 106.4% in real blood samples, and common amino acids and metal ions caused negligible fluorescence recovery. Investigation of the quenching process of CrO-B-CDs revealed that the quenching behavior is attributed to static quenching mainly induced by oxidation of surface hydroxyl groups, demonstrating that abundant surface hydroxyl groups are the key fluorescence source of B-CDs.

Future studies will compare the fluorescence generation mechanisms of carbon dots (CDs) with diverse synthesis origins and structures to verify whether the fluorescence mechanism proposed in this work is unique to B-CDs. Furthermore, the cellular imaging specificity of B-CDs will be systematically explored to clarify the universality of its imaging performance across various cell lines, so as to validate its general applicability in cellular fluorescence imaging. Finally, the Bayesian optimization strategy adopted in this work can be extended to develop other heteroatom-doped carbon-dot-based sensing platforms for the detection of biologically important small-molecule biomarkers.

Biocompatibility was assessed in a single tumor cell line (HeLa) using a metabolic-activity-based assay; evaluation in non-tumor cell lines and mechanistic studies of the uptake pathway remain to be conducted.

Supplementary Materials: The following supporting information can be downloaded at: https://www.mdpi.com/article/10.3390/molecules31234317/s1, Table S1. Comparison of reported boron doped carbon dots: precursors, quantum yields, spectral properties, and sensing performance.

Author Contributions: J.X. (Jianhao Xin): conceptualization, writing—review and editing. S.J.: writing—original draft. R.L.: investigation, formal analysis. J.W.: funding acquisition, methodology. L.L.: resources, supervision. L.F.: investigation, validation. J.X. (Jianhua Xing): funding acquisition. X.L.: software. R.P.: data curation. All authors have read and agreed to the published version of the manuscript.

Funding: This research was funded by the Henan Provincial Key Discipline Initiative, Department of Education of Henan Province (Grant No. 2023-414), the Basic Research and Applied Basic Research Program of Zhengzhou City (Grant No. ZZSZX202423), Henan Provincial Joint Training Base for Postgraduates Project (YJS2024JD57), Henan Provincial College Students' Innovation and Entrepreneurship Program (202511834039), and the Medical and Health Science and Technology Innovation Guidance Program of Zhengzhou City (Grant No. 2024YLZDJH022 and 2025YLZDJH425).

Institutional Review Board Statement: Human serum samples were collected in accordance with the ethical principles of the Declaration of Helsinki (2013 revision). The protocol was approved by the Biomedical Research Ethics Committee of Huanghe Science and Technology University (approval No. 2025–058).

Informed Consent Statement: Informed consent was obtained from all subjects involved in the study.

Data Availability Statement: All the raw datasets, including Bayesian optimization experimental data, fluorescence spectra, XPS, Raman and other characterization data, are supplied in the Supplementary Materials of this manuscript.

Conflicts of Interest: Jianhua Xing is an employee of Henan Xintai Pharmaceutical Co., Ltd. The other authors declare no conflicts of interest. Henan Xintai Pharmaceutical Co., Ltd. had no role

in the design of the study; in the collection, analyses, or interpretation of data; in the writing of the manuscript; or in the decision to publish the results.

References

1. Rezapour, R.; Arvand, M.; Habibi, M.F. A "signal-on" photoelectrochemical sensor based on hierarchical titanium dioxide nanowires/microflowers decorated graphite-like carbon nitride quantum dots for glutathione detection. *Talanta* **2025**, *285*, 127448. [CrossRef] [PubMed]
2. Xi, X.; Wang, X.; Xi, Z.; Fan, C.; Jiang, Y.; Li, Z.; Xu, L. Facile GSH-responsive glycyrrhetinic acid conjunction for liver targeting therapy. *Chin. Chem. Lett.* **2025**, *36*, 110773. [CrossRef]
3. Yang, Y.; Wu, D.; He, J.; Zheng, Q.; Mo, Y.; Jin, C.; Sheng, N.G.; Huang, F. Cu_2O-decorated MoS_2 nanoflowers with enhanced specific recognition for glutathione and its ultrasensitive electrochemical detection. *Microchem. J.* **2025**, *217*, 114998. [CrossRef]
4. Li, W.; Zhong, Y.; Zhou, P.; Li, P.; Huang, S.; Zhu, X.; Zhang, Y.; Liu, M.; Yao, S. Dual-functional silver-based metal-organic frameworks facilitate electrochemical/electrochemiluminescent dual-channel detection of chloride ions and glutathione. *Talanta* **2025**, *294*, 128278. [CrossRef] [PubMed]
5. Nishan, U.; Ullah, I.; Gul, R.; Badshah, A.; Muhammad, N.; Khan, N.; Shah, M.; Asad, M.; Afridi, S.; Ullah, R.; et al. Paracetamol-mediated synthesis of silver nanoparticles and their functionalization with ionic liquid for the colorimetric biosensing of ascorbic acid. *ACS Omega* **2023**, *8*, 44931–44941. [CrossRef] [PubMed]
6. Chen, X.; Li, N.; Lin, T.; Huang, J.; Hou, L.; Zhao, S. An off–on fluorescence sensor based on hydrogen-bonded organic frameworks for the detection of glutathione. *Microchem. J.* **2024**, *196*, 109555. [CrossRef]
7. Tan, H.; Song, Y.; Zhao, Y.; Shen, Z.; Zhao, Y.; Zhang, X.; Zhang, H. Ultrasensitive glutathione detection via competitive binding with carbon dots and gold nanoparticles on SPR chips using fluorescence microscopy–surface plasmon resonance system. *Microchem. J.* **2026**, *220*, 116596. [CrossRef]
8. Vojtovič, D.; Petřivalský, M. The optimised method of HPLC analysis of glutathione allows to determine the degree of oxidative stress in plant cell culture. *Biochem. Biophys. Res. Commun.* **2024**, *734*, 150465. [CrossRef] [PubMed]
9. Kayani, K.F.; Mohammed, S.J.; Ghafoor, D.; Rahim, M.K.; Ahmed, H.R. Carbon dot as fluorescence sensor for glutathione in human serum samples: A review. *Mater. Adv.* **2024**, *5*, 4618. [CrossRef]
10. Ai, L.; Yang, Y.; Wang, B.; Chang, J.; Tang, Z.; Yang, B.; Lu, S. Insights into photoluminescence mechanisms of carbon dots: Advances and perspectives. *Sci. Bull.* **2021**, *66*, 839–856. [CrossRef] [PubMed]
11. Sobhanan, J.; Rival, J.V.; Anas, A.; Shibu, E.S.; Takano, Y.; Biju, V. Luminescent quantum dots: Synthesis, optical properties, bioimaging and toxicity. *Adv. Drug Deliv. Rev.* **2023**, *197*, 114830. [CrossRef] [PubMed]
12. Wareing, T.C.; Gentile, P.; Phan, A.N. Biomass-based carbon dots: Current development and future perspectives. *ACS Nano* **2023**, *15*, 15471–15501. [CrossRef] [PubMed]
13. Jiang, L.; Cai, H.; Zhou, W.; Li, Z.; Zhang, L.; Bi, H. RNA-targeting carbon dots for live-cell imaging of granule dynamics. *Adv. Mater.* **2023**, *35*, 2210776. [CrossRef] [PubMed]
14. Ge, G.; Li, L.; Wang, D.; Chen, M.; Guo, C. Carbon dots: Synthesis, properties and biomedical applications. *J. Mater. Chem. B* **2021**, *9*, 6553–6575. [CrossRef] [PubMed]
15. Xu, Q.; Kuang, T.; Liu, Y.; Cai, L.; Peng, X.; Sreenivasan Sreeprasad, T.; Zhao, P.; Yu, Z.; Li, N. Heteroatom-doped carbon dots: Synthesis, characterization, properties, photoluminescence mechanism and biological applications. *J. Mater. Chem. B* **2016**, *4*, 7204–7219. [CrossRef] [PubMed]
16. Akakuru, O.; Xing, J.; Huang, S.; Iqbal, Z.; Bryant, S.; Wu, A.; Trifkovic, M. Leveraging non-radiative transitions in asphaltenes-derived carbon dots for cancer photothermal therapy. *Small* **2025**, *21*, 2404591. [CrossRef]
17. Pourmadadi, M.; Rahmani, E.; Maryam, R.K.; Samadi, A.; Behzadmehr, R.; Rahdar, A. Properties and application of carbon quantum dots (CQDs) in biosensors for disease detection: A comprehensive review. *J. Drug Deliv. Sci. Technol.* **2023**, *80*, 104156. [CrossRef]
18. Yan, F.; Zhang, H.; Xu, J.; Wu, Y.; Sun, J. Color emission carbon dots with quench-resistant solid-state fluorescence for light-emitting diodes. *ACS Sustain. Chem. Eng.* **2021**, *10*, 3901–3908. [CrossRef]
19. Mahmoud, A.Y.; Al-Masri, W. Synthesis, optical tuning, and fluorescent sensing of Fe3+ with N-doped carbon quantum dots. *Microchem. J.* **2026**, *224*, 117531. [CrossRef]
20. Peng, W.; Zheng, S.; Zhang, R.; Yi, X.; Wu, F.; Hu, J.; Ye, Y. N,P,S co-doped carbon dots as an eco-friendly and novel inhibitor for metal protection: Experimental and simulation analysis. *Colloids Surf. A* **2026**, *740*, 140155. [CrossRef]
21. Liao, L.; Luo, H.; Ouyang, H.; Wei, X.; Zhang, Z.; Ling, B.; Wang, Y.; Lv, F.; Liu, J.; Zhu, C.; et al. Many-body effects in sulfur-doped carbon nitride quantum dots: Bandgap modulation and photoluminescence tuning. *Phys. B* **2026**, *727*, 418354. [CrossRef]
22. Ustun, O.; Karadag, S.; Mazlumoglu, H.; Yilmaz, A.; Yilmaz, M. pH-Sensitive Fluorescence Emission of Boron/Nitrogen Co-Doped Carbon Quantum Dots. *Coatings* **2023**, *13*, 456. [CrossRef]

23. Ramajayam, K.; Palaniappan, A. Facile and green synthesis of highly fluorescent boron and nitrogen-doped carbon dots (BN-CDs) for the fluorimetric detection of Au3+ ions in aqueous media and in in vitro cell imaging. *Colloids Surf. A* **2025**, *709*, 136062. [CrossRef]
24. Meng, A.; Zhang, Y.; Wang, X.; Xu, Q.; Li, Z.; Sheng, L.; Yan, L. Fluorescence probe based on boron-doped carbon quantum dots for high selectivity "on-off-on" mercury ion sensing and cell imaging. *Colloids Surf. A* **2022**, *648*, 129150. [CrossRef]
25. Ramajayam, K.; Palaniappan, A. Microwave-assisted synthesis of boron/nitrogen doped highly fluorescent carbon dots for the precise detection of silver ions in real water samples and for bioimaging applications. *Inorg. Chem. Commun.* **2025**, *181*, 115124. [CrossRef]
26. Mohandoss, S.; Ahmad, N.; Rizwan Khan, M.; Sakthi Velu, K.; Kalaiselvi, K.; Palanisamy, S.; You, S.; Lee, Y.R. Multicolor emission-based nitrogen, sulfur and boron co-doped photoluminescent carbon dots for sequential sensing of Fe3+ and cysteine: RGB color sensor and live cell imaging. *Spectrochim. Acta Part A* **2023**, *302*, 123040. [CrossRef] [PubMed]
27. Meng, A.; Huangfu, B.; Sheng, L.; Hong, X.; Li, Z. One-pot hydrothermal synthesis of boron and nitrogen co-doped carbon dots for copper ion assay and multicolor cell imaging using fluorescence quenchometric method. *Microchem. J.* **2022**, *174*, 106981. [CrossRef]
28. Alqahtani, Y.S.; Mahmoud, A.M.; Ali, R.; El-Wekil, M.M. Dual-mode nanozyme sensor based on molybdenum, boron, nitrogen, and sulfur co-doped carbon dots for sensitive determination of cefoperazone in milk, serum, and pharmaceutical injections. *Microchem. J.* **2026**, *220*, 116592. [CrossRef]
29. Yang, L.; Dai, F.; Tang, H.; Li, M.; An, Y.; Tan, Y.; Liu, R.; Tan, X.; Zhang, W.; Askari Rizvi, S.F.; et al. Lophatherum-Gracile Driven near-Infrared Carbon Dots Inhibit Ferroptosis and Mitophagy to Treat Acute Kidney Injury. *Chem. Eng. J.* **2025**, *513*, 162637. [CrossRef]
30. Huang, S.; Yang, S.; Yu, L.; Ouyang, Z.; Ling, Z.; Mei, Y.; Zhang, X.; Huang, S.; Huang, Y. Mechanism-Explicit Dual-Emissive Boron/Nitrogen Co-Doped Carbon Dots for Ratiometric Detection of Fe^{3+}/Hg^{2+} via Synergistic Static Quenching Effects and Intramolecular Charge Transfer. *Colloids Surf. A* **2026**, *743*, 140598. [CrossRef]
31. Zhang, C.; Hu, Y.; Liu, H.; Zhang, X.; Luo, F.; Lou, Z.; Zhou, L.; Liang, S.; Yang, M. A boron and nitrogen co-doped carbon dot-based "on-off-on" fluorescent probe for the sequential detection of Fe^{3+} and phoxim. *Inorg. Chem. Commun.* **2026**, *192*, 117365. [CrossRef]
32. Zhao, Z.; Kubal, J.; Abraham, D.; Ryan, E. Benchmarking optimization methods for materials research: Gradient descent and Bayesian optimization for lithium-ion battery aging diagnostics. *J. Power Sources* **2025**, *656*, 238049. [CrossRef]
33. Dolar, T.; Mignerot, N.M.; Della Ventura, F.; Wang, Z.; Howard, H.C.; Kassner, C.T.; Wadley, H.N.G.; Gianola, D.S.; Chen, W. Accelerating materials discovery in heterogeneous composition-property design spaces via collaborative Bayesian optimization. *Mater. Des.* **2026**, *261*, 115331. [CrossRef]
34. Kose, Y.M.; Erturk, H. Efficiency enhancement of a thin-cell near-field thermophotovoltaic device via Bayesian optimization. *Sol. Energy Mater. Sol. Cells* **2026**, *301*, 114310. [CrossRef]
35. Liang, H.; Li, M.; Zhang, Z.; Ouyang, M.; Pei, H.; Guo, R.; Liu, N.; Mo, Z. A novel L-lysine-derived carbon dots as an "on-off-on" fluorescent sensor for efficient detection of mercury(II) and glutathione. *Appl. Surf. Sci.* **2026**, *742*, 167231. [CrossRef]
36. Han, Y.; Bian, Y.; Wang, G. A novel nitrogen-doped carbon dots as "on-off-on" fluorescent sensor for ultrasensitive and visual quantitative detection of mercury(II) and glutathione. *J. Environ. Chem. Eng.* **2023**, *11*, 110750. [CrossRef]
37. Hussain, S.A.; Mahanta, D.; Ali, A.A.; Maheswari, D.; Sadique, M.A.; Dutta, H.S.; Khan, R.; Gogoi, S. Borophene/carbon dots nanohybrid with peroxidase mimic activity for sensitive detection of glutathione. *Microchem. J.* **2025**, *218*, 115688. [CrossRef]
38. Liu, M.-X.; Zhang, X.; Liu, W.-Y.; Wang, H.-Y.; Yu, Y.-L. Coordination-driven room-temperature phosphorescent carbon dot nanozymes for dual-mode glutathione detection. *Talanta* **2025**, *290*, 127833. [CrossRef] [PubMed]
39. Khare, S.; Sohal, N.; Kaur, M.; Maity, B. Deep eutectic solvent-assisted carbon quantum dots from biomass *Triticum aestivum*: A fluorescent sensor for nanomolar detection of dual analytes mercury(II) and glutathione. *Heliyon* **2025**, *11*, e41853. [CrossRef] [PubMed]
40. Zhang, Y.; Lei, C.; Dong, P.; Fu, P.; Zhang, Y.; Hua, R. Green synthesis of carbon dots from fish scales for selective turn off–on detection of glutathione. *RSC Adv.* **2024**, *14*, 3578–3587. [CrossRef] [PubMed]
41. Gökçal, B.; Hamaloğlu, K.Ö.; Kip, Ç.; Güngör, S.Y.; Büber, E.; Tuncel, A. Glutathione detection in human serum using gold nanoparticle decorated, monodisperse porous silica microspheres in the magnetic form. *Anal. Methods* **2020**, *12*, 5219–5228. [CrossRef] [PubMed]

Disclaimer/Publisher's Note: The statements, opinions and data contained in all publications are solely those of the individual author(s) and contributor(s) and not of MDPI and/or the editor(s). MDPI and/or the editor(s) disclaim responsibility for any injury to people or property resulting from any ideas, methods, instructions or products referred to in the content.